

# TriSAM: Tri-Plane SAM for zero-shot cortical blood vessel segmentation in VEM images

Jia Wan, Wanhua Li, Jason Ken Adhinarta, Atmadeep Banerjee, Evelina Sjostedt, Jingpeng Wu, Jeff Lichtman, Hanspeter Pfister, Donglai Wei

**Abstract**—While imaging techniques at macro and mesoscales have garnered substantial attention and resources, microscale VEM imaging, capable of revealing intricate vascular details, has lacked the necessary benchmarking infrastructure. In this paper, we address a significant gap in the field of neuroimaging by introducing the largest-to-date public benchmark, BvEM, designed specifically for cortical blood vessel segmentation in volume electron microscopy (VEM) images. Our BvEM benchmark is based on VEM image volumes from three mammal species: adult mouse, macaque, and human. We standardized the resolution, addressed imaging variations, and meticulously annotated blood vessels through semi-automatic, manual, and quality control processes, ensuring high-quality 3D segmentation. Furthermore, we developed a zero-shot cortical blood vessel segmentation method named TriSAM, which leverages the powerful segmentation model SAM for 3D segmentation. To extend SAM from 2D to 3D volume segmentation, TriSAM employs a multi-seed tracking framework, leveraging the reliability of certain image planes for tracking while using others to identify potential turning points. This approach effectively achieves long-term 3D blood vessel segmentation without model training or fine-tuning. Experimental results show that TriSAM achieved superior performances on the BvEM benchmark across three species.

**Index Terms**—Blood vessel, Segment anything, Zero-shot segmentation

## I. INTRODUCTION

With around 2% of body weight, our brain receives around 20% of blood supply. Most of the energy and nutrients are consumed by the neurons, and neuron function is sensitive to the blood supply [3], [4]. The blood supply can even be adjusted following the consumption of brain regions, called neurovascular coupling [5]. Alterations of blood vessel structures are observed in many brain diseases, *e.g.*, Alzheimer’s and vascular dementia [6]. Thus, blood vessels in the brain have been extensively investigated with various imaging modalities at different resolutions (Figure 1a). Compared to the macro-level imaging (*e.g.*, CT [1] and MRI [7]) and mesoscale-

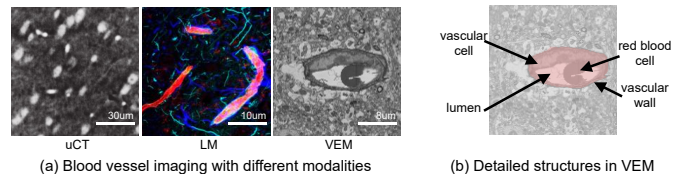


Fig. 1. Comparison of imaging modalities for blood vessel analysis. (a) Both microtomography ( $\mu$ CT) [1] and light microscopy (LM) [2] can capture sub-micron resolution of blood vessels in the cortex, but are unable to provide the ultrastructure details. (b) Volume electron microscopy (VEM) can achieve a higher resolution to show unbiased details of the vasculature including all the cell types and their cellular details.

level imaging (*e.g.*, light microscopy [2]), volume electron microscopy (VEM) [8] can further reveal the detailed ultrastructure including all vascular cells (Figure 1b) for in-depth analysis. However, no large-scale annotated VEM dataset exists to develop and evaluate automated 3D blood vessel segmentation methods.

Traditionally, the imaging methods at the macro and mesoscale are widely used and have produced a large amount of data, and a variety of image segmentation algorithms, public datasets, and evaluation methods have been developed [9], [10]. At the microscale level, the sample size of VEM is normally limited and most image analyses focus on neuron reconstruction, and blood vessels are largely ignored. Recently, owing to the rapid improvement of imaging technology, the sample size of VEM is significantly increased covering all the layers of the cerebral cortex of mouse [11] and human brain [12], as well as the whole brain of fly [13]. Moreover, imaging the whole mouse brain using VEM technology is under planning [14].

Thus, we first curate the **BvEM dataset**, the largest-to-date public benchmark dataset for cortical blood vessel segmentation in VEM images to foster segmentation method development. The raw image volumes are from recent publications, which are the largest for each of the three mammal species: mouse, macaque, and human acquired at different VEM facilities. We downsampled the volumes to a consistent resolution and performed extensive blood vessel annotation, including manual proofreading, semi-automatic segmentation error correction, and quality control, involving multiple rounds of scrutiny by neuroscience experts to ensure accuracy and completeness. However, on the BvEM dataset, existing 3D blood vessel segmentation methods suffer from two major challenges: the diversity of the image appearance due to variations in the imaging pipeline and the complexity of

Jia Wan is with the School of Computer Science and Technology, Harbin Institute of Technology (Shenzhen) (e-mail: jiiwan1998@gmail.com).

Wanhua Li and Hanspeter Pfister are with the School of Engineering and Applied Sciences, Harvard University (e-mail: {wanhua.pfister}@seas.harvard.edu).

Jason Ken Adhinarta, Atmadeep Banerjee, and Donglai Wei are with the Department of Computer Science, Boston College (e-mail: {jason.adhinarta,donglai.wei}@bc.edu).

Evelina Sjostedt and Jeff Lichtman are with the Department of Molecular and Cellular Biology, Harvard University (e-mail: {evelina\_sjostedt@fas.harvard.edu, jlichtman@mcb.harvard.edu}).

Jingpeng Wu is with the Lin Gang Laboratory (e-mail: jingpengw@lglab.ac.cn)

the 3D blood vessel morphology. Conventional blood vessel segmentation heavily depends on a substantial volume of manually annotated data, a resource that is notably scarce in the existing literature.

To address these challenges, we propose a zero-shot 3D segmentation method, **TriSAM**, leveraging the recent 2D segmentation foundation model, Segment Anything Model (SAM) [15], to handle the appearance diversity. To re-purpose SAM for 3D segmentation, we developed a multi-seed segment tracking framework based upon the video object segmentation method with SAM [16]. As it is easier to track 2D blood vessel segments along the blood flow direction, TriSAM selects the best 2D plane for SAM-based tracking and further introduces a recursive seed sampling strategy that performs tri-plane selection at the potential turning points for efficiency. Experimental results demonstrate that the proposed TriSAM method significantly outperforms the prior state-of-the-art methods on the proposed BvEM benchmark across all three species.

## II. RELATED WORK

**Blood Vessel Segmentation.** Most existing VEM image segmentation algorithms were developed for neurons [17] and synapses [18]–[20]. The traditional VEM dataset size is too small to study blood vessel architecture. Recently, with rapid technology improvement, VEM sample size reached the cubic millimeter scale covering all the layers of cerebral cortex [11], [12]. This marks a significant milestone in connectomics research. The blood vessels were segmented manually in the human cortex [12] and automatically using fully convolutional neural network (FCN) [21] or 3D U-Net [11], [22], [23]. Due to the burden of annotation, efforts have been made to decrease the need for annotations [24]. For images acquired using other related imaging methods, such as light microscopy and MRI, many methods were developed and covered by some reviews [9], [10]. Briefly, the blood vessels could be enhanced based on the nature of tubeness using filters like diffusion and ridge filtering. Yet, the segmentation of cortical blood vessels in VEM images is seldom explored due to the absence of publicly available benchmarks.

**Evaluation Metrics.** Quantitative evaluation is normally conducted by comparing with manual annotations that are used as the ground truth. The evaluation metrics could be classified into two categories: pixel-based and skeleton-based [10]. Pixel-based metrics measure the difference between segmentation and ground truth at the pixel or voxel level, such as Accuracy and Dice Similarity Coefficient [25]. Skeleton-based metrics measure the difference of skeletons or centerlines, such as Overlap and Overlap Until First Error [26]. Skeleton-based metric requires the blood vessel skeleton that might not always be available. It also requires the computation of point-to-point correspondence between the ground truth and computed skeletons. All existing evaluation metrics are developed using datasets acquired using other imaging methods and we did not find any specific metric for VEM datasets. Most of them could be utilized in VEM images directly. Here we adopt the metrics Precision, Recall, and Accuracy as we measure instance-level pixel prediction.

**Segment Anything-Based Models.** As a foundation model for image segmentation, the recently proposed Segment Anything Model [15] has garnered significant attention and has been extended to a variety of domains [27]–[30] including object tracking [16], [27], image inpainting [28], image matting [31], super-resolution [32], 3D point cloud [33], and image editing [34]. Despite SAM’s remarkable generalization capabilities, it still encounters some challenges in practical applications. One of these challenges is the huge computation costs due to the heavyweight image encoder. FastSAM [35] adopted a conventional CNN detector with an instance segmentation branch for the segment anything task with real-time speed. MobileSAM [36] proposed decoupled distillation to obtain a small image encoder, which achieved approximately five times faster speed compared to FastSAM while also being seven times smaller in size. Therefore the MobileSAM is employed in our proposed method. One important challenge lies in the unsatisfactory performance of SAM when confronted with special domains, such as medical [37] or biological [38] images, particularly in the context of 3D data. Although SAM demonstrates impressive generalization capabilities, it faces challenges in specialized domains like medical [37], [39] or biological images [38], especially in handling 3D data. [30] assessed the SAM model’s zero-shot segmentation performance in the context of digital pathology and showed scenarios where SAM encounters difficulties. [40] extensively evaluates the SAM for medical image segmentation across 19 diverse datasets, highlighting SAM’s performance variability. To address the domain gap between natural and medical images, SAM-Adapter [37], SAM-Med2D [41], and Medical SAM Adapter [42] introduced Adapter modules and trained the Adapter with medical images. They attained good performance on various medical image segmentation tasks. MedSAM [29] adapted SAM with more than one million medical image-mask pairs and attained accurate segmentation results. MicroSAM [38] also presented a segment anything model for microscopy by fine-tuning SAM with microscopy data. Unlike these approaches that require model fine-tuning for adaptation, our method lifts the blood vessel segmentation capabilities of SAM from 2D images to 3D volumes without any model fine-tuning.

## III. BVEM DATASET

### A. Sample Information

We built the BvEM dataset upon the largest publicly available VEM image volumes for three mammal species: visual cortex from an adult mouse<sup>1</sup> [11], superior temporal gyrus from an adult macaque [43], and temporal lobe from an adult human [12]. Each volume was acquired with different protocols at different facilities and we refer to respective papers for more details.

### B. Image Volume Standardization

We first downsampled all three VEM image volumes to a near-isotropic resolution ( $\sim 200$ - $300$  nm) along each dimension, which is a good balance between rich image details

<sup>1</sup>BvEM-Mouse can be visualized in: <https://tinyurl.com/yc2s38x9>

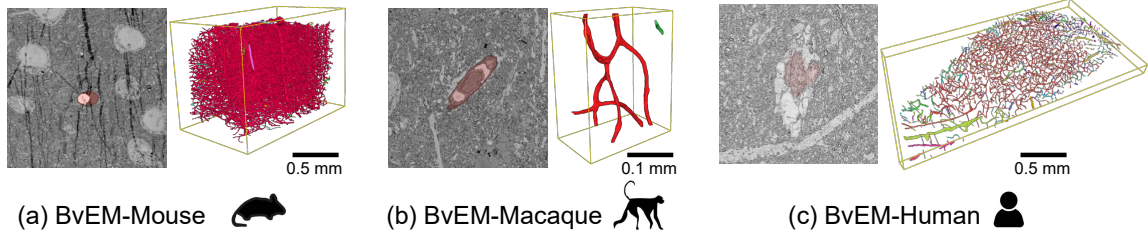


Fig. 2. The proposed BvEM dataset. We proofread the blood vessel instance segmentation (displayed in different colors) in the three largest publicly available VEM volumes: (a) mouse [11], macaque [43], and human [12] samples acquired at different VEM labs.

TABLE I

DATASET INFORMATION. DESPITE THE DIFFERENCE IN THE SCALE AND THE GEOMETRY OF THE IMAGE VOLUME, THE LARGEST BLOOD VESSEL INSTANCE (RENDERED IN RED) IS SIGNIFICANTLY BIGGER THAN THE REST COMBINED. THE LAST COLUMN SHOWS THE MAX/TOTAL LENGTH OF THE BLOOD VESSEL INSTANCES.

Sample	Resolution (nm)	Size (voxel)	Length: (mm)
Mouse (TEM)	320 × 256 × 256	2495 × 3571 × 2495	1.6/1.7
Macaque (SBEM)	240 × 176 × 176	450 × 1271 × 995	713.3/714.5
Human (MultiSEM)	264 × 256 × 256	661 × 7752 × 13500	107.2/126.7

for biological analysis and a manageable dataset size for AI researchers. Then, we trimmed the image boundary of the BvEM-Mouse and BvEM-Human volumes, where the blood vessels are hard to annotate due to the missing image content. As shown in Fig. 2, the imaging quality and the appearance of blood vessels vary drastically across these three volumes, showcasing the cutting-edge large-scale VEM imaging pipelines.

### C. Blood Vessel Instance Segmentation Annotation

(1) *Initial annotation.* The paper on the BvEM-human volume provides a manual proofread blood vessel segmentation, where many segments are incomplete or disconnected due to missing annotations. The papers for BvEM-mouse and BvEM-macaque volumes only provide dense 3D instance segmentation and we manually selected the blood vessel segments. Due to the large scale of the BvEM-Mouse and BvEM-Human volumes, we only annotated every 4 slices, where the z-dimension resolution is around  $1\mu\text{m}$ . (2) *Semi-automatic segmentation error correction.* We used the VAST lite software [44] which can accelerate the proofreading process by using provided segmentation results as the drawing or filling template instead of delineating segments manually. (3) *Quality control.* We used 3D visualizations and skeleton analysis to detect remaining segmentation errors. Each volume was proofread by two neuroscience experts in multiple rounds until no disagreement.

### D. Dataset Statistics

We summarize the dataset details in Tab. I. The BvEM-Macaque volume has around 0.5G voxels, and the BvEM-Mouse and BvEM-Human volumes are around 80 and 121 times bigger, respectively. From the blood vessel instance

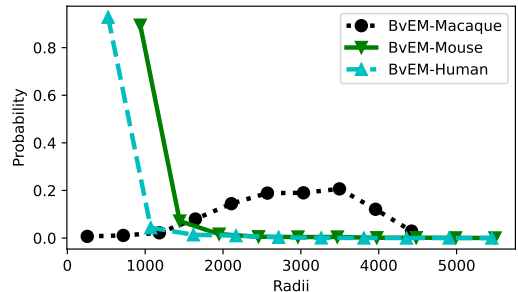


Fig. 3. Dataset statistics: the histogram of the blood vessel radius.

segmentation annotation, we automatically extracted skeleton centerlines [45] and computed the length for each blood vessel instance. Due to the hyper-connectivity nature of cortical blood vessels, the length of the largest instance is around 99%, 95%, and 85% for each volume. The histogram of the blood vessel radius in the proposed dataset is shown in Figure 3 where the dimension is in the “zyx” order.

## IV. METHOD

### A. Overview

We formulate the 3D blood vessel segmentation task as a multi-seed video object segmentation task: generating one 3D segment per seed through tracking 2D SAM results along one fixed direction and the final output is the connected component of the combined segmentation results (Fig. 5a). However, unlike videos, the 3D blood vessel segment can be tracked from different axes, whereas 2D SAM segmentation results can be of drastically different qualities. As shown in Fig. 5b, the seed generation can have many errors leading to incomplete segmentation results. To achieve long-term tracking, the framework needs a *recursive seed sampling* module to propose potential turning points as new seeds based on segmentation results. As shown in Fig. 5c, the ground truth segment on some 2D planes can have such an unnatural shape that SAM fails to segment it, not to mention its drastic shape change along the axis. Ideally, one axis is along the blood flow direction where the 2D tracking plane is an ellipse shape, e.g., zx plane in the example. Thus, it is essential to have a *tri-plane selection* module in the framework.

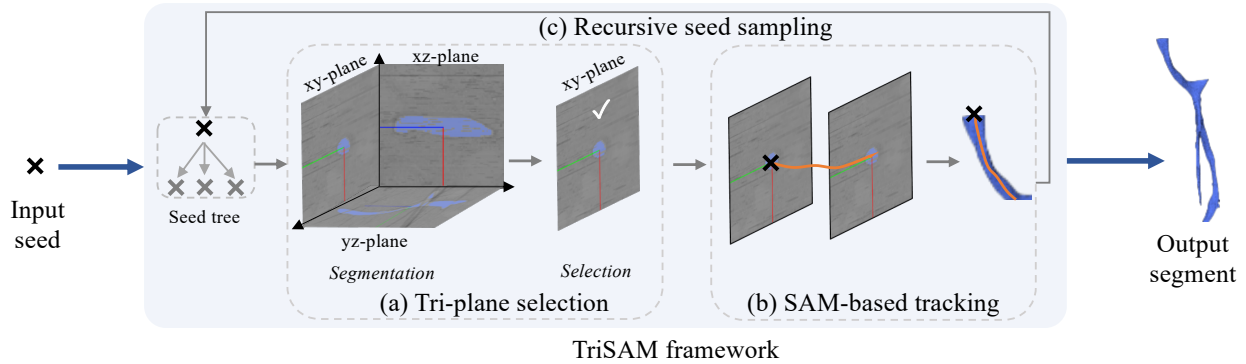


Fig. 4. TriSAM framework. (a) Tri-plane selection is first proposed to select the best plane for tracking. (b) SAM-based tracking leverages SAM to perform short-term tracking given a seed location and a tracking direction. (c) Recursive seed sampling exploits potential turning points for long-term tracking.

The proposed TriSAM framework has the following three modules: tri-plane selection, SAM-based tracking, and recursive seed sampling (Fig. 4).

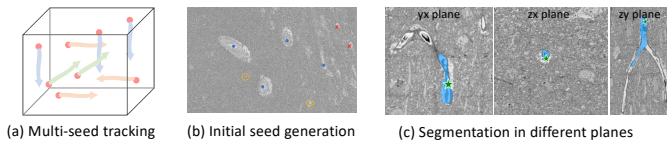


Fig. 5. Problem formulation and challenges. (a) The 3D segmentation task can be formulated as the multi-seed object tracking problem. There are two main challenges for such an approach: (b) generating high-quality initial seeds (blue dots) and minimizing the false positive (red crosses) and false negative errors (yellow circles); (c) adaptively selecting tracking directions as the quality of SAM segmentation results can vary significantly.

### B. Tri-Plane Selection

Rather than videos, 3D VEM images can be interpreted in different planes. In practice, tracking along some of the planes is hard since the shape and scale of the blood vessels change dramatically. This phenomenon can be further confirmed by the experiment shown in Table III in which tracking along the  $y$  axis is more effective than tracking along the  $x$  axis. Given the seed position as a prompt, we run SAM on each of the tri-planes of the 3D image volume centered at the seed. Note that the plane that is most tangent to the blood flow direction has the smallest segment size, capturing the blood vessel’s cross-section (Fig. 4a,  $xy$ -plane). In addition, SAM outputs the probability for the segment result, reflecting the confidence of the naturalness of its shape. Thus, to combine the above cues for tri-plane selection, we pick the 2D plane with the smallest segment size and a probability higher than the threshold  $\tau$ . TriSAM terminates when no plane is selected.

### C. SAM-based Tracking

Given the segment on the selected 2D plane from above, we aim to track it with SAM along the orthogonal axis. If we use the center of the current segment as the point prompt for the next slice, SAM may output segments with inconsistent sizes along the axis due to the lack of size information in the point prompt. If we use the bounding box of the current segment

as the box prompt, SAM may not track in the long term as the output enclosed in the bounding box is getting smaller and smaller. Empirically, we find prompting SAM with both the enlarged bounding box and the center of the segment generates better segment tracking results. TriSAM terminates when SAM returns no prediction for the next image slice.

### D. Recursive Seed Sampling

The above modules work well when the blood vessel travels in one direction. In reality, blood vessels not only turn in different directions but also bifurcate, leading to drastic shape and scale changes as shown in Fig. 11. Thus, we need a module to propose potential turning points to recursively run TriSAM, linking short-term segment tracks into long-term segment tracks. SAM-based tracking is simple and fast for short-term tracking. But it may fail when shape and scale change dramatically as shown in Fig. 11. Therefore, it relies on the large number of seeds which is hard to generate as shown in Fig. 5(b).

To enable long-term tracking, we propose a recursive seed sampling method to exploit the 3D blood vessel structure, which keeps track of potential turning points in blood vessels. Given the 3D segment from the short-term track after TriSAM terminates, we first use the Farthest Point Sampling (FPS) to find potential endpoints. Then, we add these points to the global seed tree whose root node is the input seed. To avoid repeating the track along the same direction as the previous short-term track, these newly sampled seeds store the previous tracking direction. For example, if the previous track is along the  $z$ -axis, TriSAM on the new seed will not compute results along the  $z$ -axis to encourage exploration of new tracking directions. During each iteration, we take an unvisited node in the seed tree, mark it as visited, and run TriSAM along a different tracking direction. With such a seed tree data structure, we run TriSAM recursively until all potential points are visited. For each endpoint, we re-run the above two TriSAM modules to track segments along directions that are different from the current tracking axis.

Mathematically, we denote the 3D coordinate of a turning point as  $(x_t, y_t, z_t)$ . At this point, we perform the SAM operation on three planes separately. We use  $M_z(x, y, z_t)$ ,  $M_y(x, y_t, z)$ , and  $M_x(x_t, y, z)$  to represent the segmented

**Algorithm 1** TriSAM algorithm

---

**Require:** 3D volume  $\mathbf{X}$  and a sample seed  $s$ , a threshold  $\tau$

Initialize the prediction  $\mathbf{P} = \mathbf{0}$

Initialize the seed tree  $SeedTree = s$

**for**  $t_i$  *in*  $RemainNode(SeedTree)$  **do**

$plane = Select(\mathbf{X}, t_i)$   $\triangleright$  Select the best tracking plane

$segment = SAMBasedTrack(\mathbf{X}, t_i, plane)$

$\mathbf{P} = Update(\mathbf{P}, segment)$   $\triangleright$  Add the segment to  $\mathbf{P}$

$Seeds = RecursiveSample(\mathbf{X}, t_i)$   $\triangleright$  Generate seed from potential turning points

**if**  $Valid(Seeds)$  **then**

$SeedTree = LeafSplit(SeedTree, t_i, Seeds)$   $\triangleright$

Grow the seed tree

**end if**

**end for**

**return**  $\mathbf{P}$

---

mask region along xy plane, xz plane, and yz plane, respectively. Assuming that the chosen best plane is xz plane which means we will track along the y-axis, we will obtain new turning points based on the segmented masks on the non-best planes  $M_z(x, y, z_t)$  and  $M_x(x_t, y, z)$ . Since the boundary region of the mask corresponds to where blood vessels disappear, it indicates locations where there is a change in the direction of blood vessel flow. So, the boundaries in the y-direction of both  $M_z(x, y, z_t)$  and  $M_x(x_t, y, z)$  indicate locations where blood vessels change direction along the y-axis. We further define the maximum and minimum values of the y-coordinate within the  $M_z(x, y, z_t)$  region as  $y_{max}^{z_t}$  and  $y_{min}^{z_t}$ , respectively. Similarly, we can define  $y_{max}^{x_t}$  and  $y_{min}^{x_t}$ . Then the new turning points can be defined as  $\{(x, y, z) | (x, y, z) \in M_z(x, y_{max}^{z_t}, z_t) \cup M_z(x, y_{min}^{z_t}, z_t) \cup M_x(x_t, y_{max}^{x_t}, z) \cup M_x(x_t, y_{min}^{x_t}, z)\}$ . The turning point will be dropped if it hits the volume boundary or the probability of its segment is less than the threshold  $\tau$ . After updating the turning point tree, we then sample a new leaf node for the next iteration until all leaf nodes are sampled.

In practice, we maintain a tree of seed points where the root is the initial seed. In each iteration, we sample a left node in the tree, mark it as visited, and run TriSAM. Empirically, we find the non-best planes potentially identify turning points or endpoints accurately. Therefore, we propose to generate the turning points according to the segmentation results at non-best planes. Potential turning points are identified as points in these segments with the smallest and largest z-values. The algorithm of TriSAM is shown in Algorithm 1.

## V. EXPERIMENTS

In this section, we present TriSAM’s experimental results. We begin with settings and implementation details. Then we show the benchmark results. Finally, we perform ablations for further analysis.

### A. Experimental Settings

**Implementation Details.** Since the volume is too large, non-overlapping subvolumes are used for segmentation and the

results are fused to form the final prediction. Initial seeds can be effectively generated with global color thresholding since the pixels of blood vessels are brighter than the background. Therefore, pixels darker than a threshold are considered as background while others are seed candidates. To improve efficiency, we only keep the center of each connected component as the final seeds. For BvEM-Macaque, we directly predict the whole volume. For others,  $k \times 1024 \times 1024$  subvolumes are used since it is the default resolution for SAM where  $k = 661$  for BvEM-Human and  $k = 818$  for BvEM-Mouse. For preprocessing, we utilize deflickering method and temporal smoothing on the z-axis to remove the artifacts and missing slices. For postprocessing, holes are filled and small connected components are removed after the segmentation. Global color thresholding is used to generate the initial seeds and  $\eta$  is set to 0.98 as shown Fig. 8 (left). Given the significantly greater complexity of human blood vessels, we employ the manually generated seeds for the challenging BvEM-Human volume. For SAM-based tracking, the probability threshold  $\tau$  is set to 0.8. according to the experiment shown in Fig. 8 (right). Unless explicitly stated otherwise, we use MobileSAM [36] instead of the standard SAM [15] in all conducted experiments to improve the inference speed. All experiments are conducted on an NVIDIA-A100 GPU.

**Evaluation Metrics.** We use the Precision, Recall, and Accuracy metric defined in [46], where  $Accuracy = \frac{TP}{TP+FP+FN}$ .

$$Precision = \frac{TP}{TP + FP}, \quad (1)$$

$$Recall = \frac{TP}{TP + FN}, \quad (2)$$

$$Accuracy = \frac{TP}{TP + FP + FN}, \quad (3)$$

where  $TP$ ,  $FP$ , and  $FN$  are instance-level true positive, false positive, and false negative respectively. We use instance-level metrics since it is more sensitive to split errors. In particular, the Hungarian algorithm is used to match ground-truth instances and predicted instances with negative Accuracy as the cost matrix. We used the whole dataset for evaluation and computed the score on the largest instance segment of each volume due to its dominating size.

### B. Benchmark Results

**Methods in Comparison.** We compare the proposed TriSAM with both zero-shot baselines and supervised methods. The compared zero-shot methods are global color thresholding and SAM+IoU tracking. For color thresholding, we first perform (3D) Gaussian blurring with  $\sigma = 1$  on 3D chunks ( $10 \times 512 \times 512$ ). Then we label all voxels that are 3 standard derivations above mean as positive. Finally, connected components with less than 1000 voxels are filtered out. For SAM+IoU Tracking, we segment all objects in each z-slice of the dataset using automatic mask generation. Then we track each blood vessel using the first labeled slice as seeds. Our simple tracking algorithm finds the mask in the next slice with maximum IoU with the current slice. If the max IoU is above a threshold, we assign this mask to the current object and continue tracking. We also tried SAM+IoU tracking with

TABLE II  
BENCHMARK RESULTS ON THE PROPOSED BVEM DATASET. WE EVALUATE THE INITIAL BLOOD VESSEL ANNOTATION TO SHOW THE SIGNIFICANT AMOUNT OF OUR PROOFREADING EFFORT.

Method	Setting	BvEM-Mouse			BvEM-Macaque			BvEM-Human		
		Pre	Rec	Acc	Pre	Rec	Acc	Pre	Rec	Acc
Initial annotation	N/A	93.74	36.62	35.74	1.65	23.17	1.57	100.00	25.68	25.68
Color thresholding	N/A	<b>86.45</b>	37.32	35.26	<b>95.14</b>	21.65	21.42	<b>41.77</b>	1.92	1.87
MAESTER [47]	unsupervised	2.16	18.95	0.94	22.08	40.30	16.64	0.29	5.03	0.27
3D UNet [11]	supervised	13.45	0.91	0.67	16.56	86.95	16.16	68.63	2.46	2.43
nnUNET [48]	supervised	3.54	49.55	6.59	24.34	29.57	23.74	3.44	23.20	5.86
SAM+IoU tracking	zero-shot	63.59	0.27	0.27	74.39	1.89	1.88	18.19	23.58	12.92
<b>TriSAM (ours)</b>	zero-shot	84.12	<b>66.75</b>	<b>59.28</b>	78.41	<b>74.97</b>	<b>62.14</b>	31.35	<b>25.57</b>	<b>16.39</b>



Fig. 6. Qualitative instance segmentation results on the BvEM-Macaque volume. Different colors indicate different instances. Color thresholding and 3D UNet often produce false positives, whereas SAM+IoU tracking tends to miss a significant portion of blood vessels. Among the comparison methods, TriSAM segmentation stands out as the most effective.

microSAM [49] weights that have been finetuned on EM images. This model however does not work well on our dataset. We expect this is because microSAM has been finetuned on high-resolution EM images and does not generalize to our low-resolution dataset. We further compare TriSAM with the supervised method 3D U-Net [11]. We use the implementation from [50]. For supervised methods, we cropped subvolumes at the center of each volume composing approximately 10% in size. These annotated subvolumes were divided into a 1-1 train-val split.

**Results Analysis.** The results are shown in Tab. II. First, both the Color Thresholding and SAM+IoU Tracking methods exhibit significant performance variability across three volumes, highlighting the diversity of our dataset and the sensitivity of these methods to different species. Furthermore, both of these unsupervised methods demonstrate relatively poor performance, underscoring the challenges of the zero-shot setting in the BvEM dataset. Additionally, the 3D UNet, as a supervised learning approach, also yields subpar results, indicating poor generalization of models trained with limited data. Finally, TriSAM significantly outperforms other methods as it not only accurately segments the boundary but also tracks the blood vessels in the long term.

**Qualitative Results.** The final instance segmentation results on BvEM-Macaque are shown in Fig. 6. Color thresholding segments bright pixels, inadvertently capturing nuclei cells while overlooking darker pixels corresponding to blood vessels. Training the 3D UNet model with limited data results in confusion with background elements. IoU tracking fails to

capture a significant portion of the blood vessel, revealing its ineffectiveness in tracking. TriSAM prediction emerges as the most accurate method, affirming its effectiveness.

### C. Ablation Studies

We conducted a comprehensive series of ablation studies exclusively using the BvEM-Macaque dataset due to the computation constraints.

**Effect of the Tri-plane Selection.** We first compare our method with the single-plane methods to evaluate the effectiveness of the tri-plane. For the single-plane method, we choose one plane as the main plane and only track along the chosen plane. The results on the BvEM-Macaque volume are shown in Tab. III. We have observed significant differences in performance among the three single-plane methods, with accuracy ranging from 11.53% to 50.75%, depending on the chosen tracking plane, which indicates the importance of the chosen tracking plane. This variability can be attributed to the tubular nature of blood vessel extensions within biological organisms, resulting in the generation of intricate mask shapes in certain planes, while simpler mask shapes are produced in others. Then we fuse the results of three Single-Plane methods and attain a higher accuracy of 57.41%, which demonstrates that the segmentation results from different planes exhibit a high degree of complementarity with each other. Instead, We see that tri-plane selection exploits the blood vessel 3D structures by tracking along a suitable plane and attains the highest accuracy of 62.14%.

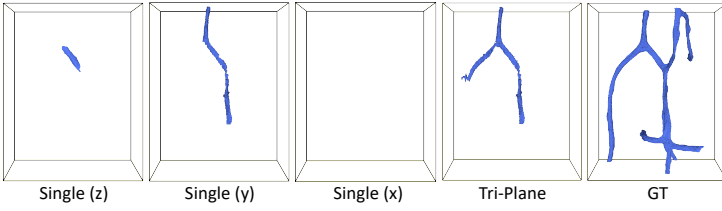


Fig. 7. Segmentation results with different plane selection strategies.

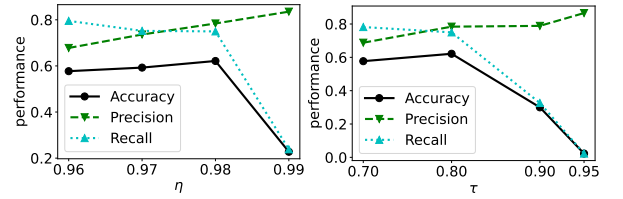


Fig. 8. Ablation study results on hyperparameters  $\eta$  and  $\tau$ .

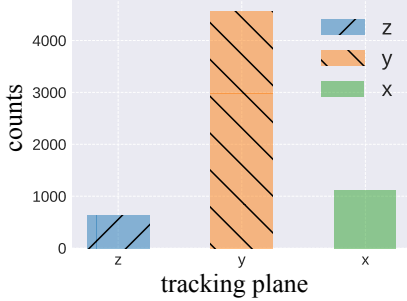


Fig. 9. Histogram of the tri-plane selection.

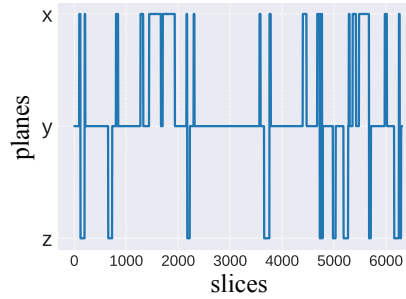


Fig. 10. Dynamics of the tri-plane selection.

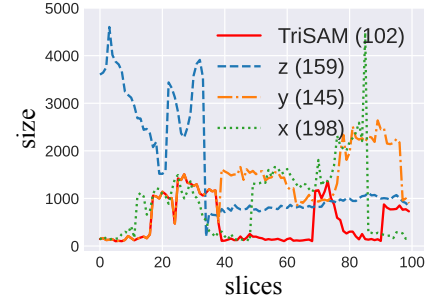


Fig. 11. Dynamics of segment size.

TABLE III  
ABLATION STUDIES ON DIFFERENT PLANE SELECTION STRATEGIES. THE PROPOSED TRI-PLANE APPROACH ACHIEVES THE BEST OVERALL ACCURACY WITH COMPARABLE SPEED.

Method	Pre. (%)	Rec. (%)	Acc. (%)	Speed (sec)
Single-plane (z)	75.28	48.48	41.82	324
Single-plane (y)	<b>79.37</b>	58.47	50.75	<b>307</b>
Single-plane (x)	69.73	12.14	11.53	345
Single-plane (fusion)	71.78	74.15	57.41	976
<b>Tri-plane</b>	78.41	<b>74.97</b>	<b>62.14</b>	335

TABLE IV  
ABLATION STUDIES ON DIFFERENT SEED SAMPLING STRATEGIES. THE PROPOSED RECURSIVE SEED SAMPLING APPROACH ACHIEVES THE BEST OVERALL ACCURACY WITH COMPARABLE SPEED.

Strategy	Pre. (%)	Rec. (%)	Acc. (%)	Speed (sec)
Naive	79.37	58.47	50.75	<b>307</b>
Dense sampling	<b>86.94</b>	24.84	23.95	2001(↑ 552%)
<b>Recursive sampling</b>	78.41	<b>74.97</b>	<b>62.14</b>	335 (↑ 9%)

We visualize the segmentation results with one initial seed on BvEM-Macaque in Fig. 7. The origin point is the seed location. We see that the performance is sensitive to the selection of the tracking plane. If the plane is not well-selected, the segmentation result can be empty as the example of tracking along the x-axis shows. The best result is tracking along the y-axis which is still worse than the proposed method since it considers potential turning points to leverage the 3D structure. The best result is tracking along the y-axis. However, it still falls short of the proposed method’s performance, as the latter takes into account potential turning points to exploit the 3D structure and perform long-term tracking.

**Effect of the Recursive Redirection Strategy.** To perform long-term tracking and fully leverage the 3D blood vessel structure, we introduced recursive seed sampling by considering potential turning points. To validate its effectiveness, we report the results on the BvEM-Macaque volume in Tab. IV

TABLE V  
ABLATION STUDY RESULTS ON THE CHOICE OF SAM MODELS. THE MOBILESAM MODEL ACHIEVES BETTER PERFORMANCE WITH FASTER INFERENCE SPEED AND SMALLER MODEL SIZE.

Backbone	Pre (%)	Rec (%)	Acc (%)	Speed	Parameters
SAM [15]	77.65	66.03	55.48	1535s	615M
MobileSAM [36]	<b>78.41</b>	<b>74.97</b>	<b>62.14</b>	<b>335s</b>	<b>9.66M</b>

where the runtime comparison for segmentation prediction on the entire BvEM-Macaque data is also included. Compared to the baseline without recursive seed sampling “naive” and dense seed sampling “dense”, the proposed method achieves the best performance with less than 10% running time increase. One naive baseline is to remove the recursive seed sampling component and not consider any potential turning points. This strategy is simple and fast but it fails to exploit the 3D shape prior leading to poor performance. Another strategy is to select the best plane for every tracking step/slice, which densely performs SAM segmentation on each step across three planes. Therefore, the performance is limited. The proposed method achieves the best performance with less than 10% running time increase on the BvEM-Macaque dataset. Unfortunately, it significantly increases the computation cost. Compared to our method, DenseSAM’s running time is 5.97 times longer since it needs to segment 3 planes for every tracking step. However, we were surprised to observe that the performance of the Dense Redirection strategy was even worse. This could be attributed to the frequent axis changes potentially leading to the omission of certain parts of the blood vessel and causing splitting errors.

**Quality Analysis.** We delve deeper into the plane dynamics in Fig. 9 and 10. The majority of the selected plane predominantly tracks along the y-axis. This observation aligns with the experimental results presented in Tab.III, where it is evident that a single plane tracking with the y-axis outperforms the z-

axis and x-axis. This is because the blood vessel flows mainly along the y-axis in the test volume. In Fig. 11, we explore the size dynamics using various methods, where the mean derivation is shown in parentheses. The size variation observed with our proposed method is relatively smaller compared to tracking along the y-axis and significantly less than when tracking along the z-axis and x-axis.

**Other Ablations.** To further improve the efficiency, we use MobileSAM instead of the original SAM in practice. As shown in Table V, the inference time of MobileSAM is 22% of the original SAM which confirms that MobileSAM significantly improves the inference speed. Moreover, the performance of MobileSAM is even better than the original SAM, possibly because the distilled small model is less prone to overfitting to the original natural image domain. Fig. 8 illustrates the performance with varying hyperparameters  $\eta$  and  $\tau$ .

#### D. Failure Cases

Despite our method's significant progress, it still encounters challenges in some scenarios, as illustrated in Figure 12. The first issue is the seed problem, where the presence of a false positive seed can lead to erroneous predictions. Secondly, SAM could also fail to segment the mask. Lastly, tracking failure tends to occur at blood vessel junction points. These instances highlight the complexity of tracking in such intricate vascular networks and suggest the need for further refinements in our approach to address these specific failure cases effectively.

## VI. CONCLUSION

In this paper, we contribute the largest-to-date public benchmark, the BvEM dataset, for cortical blood vessel segmentation in 3D VEM images. We also developed a zero-shot blood vessel segmentation method, TriSAM, based on the powerful SAM model, offering an efficient and accurate approach for segmenting blood vessels in VEM images. With tri-plane selection, SAM-based tracking, and recursive seed sampling, our TriSAM effectively exploits the 3D blood vessel structure and attains superior performance compared with existing zero-shot and supervised technologies on BvEM across three species, marking a critical step towards unlocking the mysteries of neurovascular coupling and its implications for brain health and pathology. With the availability of the BvEM dataset and the TriSAM method, researchers are now equipped with valuable tools to drive breakthroughs in VEM-based cortical blood vessel segmentation and further our understanding of the brain's intricate vascular network. By addressing a significant gap in the field of neuroimaging, we have laid the foundation for advancing the understanding of cerebral vasculature at the microscale and its intricate relationship with neural function.

## REFERENCES

- [1] E. L. Dyer, W. G. Roncal, J. A. Prasad, H. L. Fernandes, D. Gürsoy, V. De Andrade, K. Fezzaa, X. Xiao, J. T. Vogelstein, C. Jacobsen *et al.*, "Quantifying mesoscale neuroanatomy using x-ray microtomography," *neuro*, vol. 4, no. 5, 2017.
- [2] J. J. Lochhead, E. I. Williams, E. S. Reddell, E. Dorn, P. T. Ronaldson, and T. P. Davis, "High resolution multiplex confocal imaging of the neurovascular unit in health and experimental ischemic stroke," *Cells*, vol. 12, no. 4, p. 645, 2023.
- [3] B. J. Andreone, B. Lacoste, and C. Gu, "Neuronal and vascular interactions," *Annual review of neuroscience*, vol. 38, pp. 25–46, 2015.
- [4] A. Peters, U. Schweiger, L. Pellerin, C. Hubold, K. Oltmanns, M. Conrad, B. Schultes, J. Born, and H. Fehm, "The selfish brain: competition for energy resources," *Neuroscience & Biobehavioral Reviews*, vol. 28, no. 2, pp. 143–180, 2004.
- [5] C. Iadecola, "Neurovascular regulation in the normal brain and in alzheimer's disease," *Nature Reviews Neuroscience*, vol. 5, no. 5, pp. 347–360, 2004.
- [6] R. N. Kalaria, "Vascular basis for brain degeneration: faltering controls and risk factors for dementia," *Nutrition reviews*, vol. 68, no. suppl\_2, pp. S74–S87, 2010.
- [7] D. M. McDonald and P. L. Choyke, "Imaging of angiogenesis: from microscope to clinic," *Nature medicine*, vol. 9, no. 6, pp. 713–725, 2003.
- [8] C. J. Peddie, C. Genoud, A. Kreshuk, K. Meechan, K. D. Micheva, K. Narayan, C. Pape, R. G. Parton, N. L. Schieber, Y. Schwab *et al.*, "Volume electron microscopy," *Nature Reviews Methods Primers*, vol. 2, no. 1, p. 51, 2022.
- [9] M. R. Goni, N. I. R. Ruhaiyem, M. Mustapha, A. Achuthan, and C. M. N. C. M. Nassir, "Brain vessel segmentation using deep learning—a review," *IEEE Access*, 2022.
- [10] S. Moccia, E. De Momi, S. El Hadji, and L. S. Mattos, "Blood vessel segmentation algorithms—review of methods, datasets and evaluation metrics," *Computer methods and programs in biomedicine*, vol. 158, pp. 71–91, 2018.
- [11] The MICrONS Consortium, J. A. Bae, M. Baptiste, C. A. Bishop, A. L. Bodor, D. Brittain, J. Buchanan, D. J. Bumbarger, M. A. Castro, B. Celii, E. Cobos, F. Collman, N. M. da Costa, S. Dorkenwald, L. Elabbady, P. G. Fahey, T. Fliss, E. Froudarakis, J. Gager, C. Gamlin, W. Gray-Roncal, A. Halageri, J. Hebditch, Z. Jia, E. Joyce, J. Joyce, C. Jordan, D. Kapner, N. Kemnitz, S. Kinn, L. M. Kitchell, S. Koolman, K. Kuehner, K. Lee, K. Li, R. Lu, T. Macrina, G. Mahalingam, J. Matelsky, S. McReynolds, E. Miranda, E. Mitchell, S. S. Mondal, M. Moore, S. Mu, T. Muhammad, B. Nehoran, O. Ogedengbe, C. Papadopoulos, S. Papadopoulos, S. Patel, X. Pitkow, S. Popovych, A. Ramos, R. C. Reid, J. Reimer, P. K. Rivlin, V. Rose, C. M. Schneider-Mizell, H. S. Seung, B. Silverman, W. Silversmith, A. Sterling, F. H. Sinz, C. L. Smith, S. Suckow, M. Takeno, Z. H. Tan, A. S. Tolias, R. Torres, N. L. Turner, E. Y. Walker, T. Wang, A. Wanner, B. A. Wester, G. Williams, S. Williams, K. Willie, R. Willie, W. Wong, J. Wu, C. Xu, R. Yang, D. Yatsenko, F. Ye, W. Yin, R. Young, S. chieh Yu, D. Xenos, and C. Zhang, "Functional connectomics spanning multiple areas of mouse visual cortex," *bioRxiv*, 2023. [Online]. Available: <https://www.biorxiv.org/content/early/2023/04/19/2021.07.28.454025>
- [12] A. Shapson-Coe, M. Januszewski, D. R. Berger, A. Pope, Y. Wu, T. Blakely, R. L. Schalek, P. H. Li, S. Wang, J. Maitin-Shepard *et al.*, "A connectomic study of a petascale fragment of human cerebral cortex," *BioRxiv*, pp. 2021–05, 2021.
- [13] S. Dorkenwald, A. Matsliah, A. R. Sterling, P. Schlegel, S. chieh Yu, C. E. McKellar, A. Lin, M. Costa, K. Eichler, Y. Yin, W. Silversmith, C. Schneider-Mizell, C. S. Jordan, D. Brittain, A. Halageri, K. Kuehner, O. Ogedengbe, R. Morey, J. Gager, K. Kruk, E. Perlman, R. Yang, D. Deutsch, D. Bland, M. Sorek, R. Lu, T. Macrina, K. Lee, J. A. Bae, S. Mu, B. Nehoran, E. Mitchell, S. Popovych, J. Wu, Z. Jia, M. Castro, N. Kemnitz, D. Ih, A. S. Bates, N. Eckstein, J. Funke, F. Collman, D. D. Bock, G. S. Jefferis, H. S. Seung, M. Murthy, and the FlyWire Consortium, "Neuronal wiring diagram of an adult brain," *bioRxiv*, 2023. [Online]. Available: <https://www.biorxiv.org/content/early/2023/07/11/2023.06.27.546656>
- [14] L. F. Abbott, D. D. Bock, E. M. Callaway, W. Denk, C. Dulac, A. L. Fairhall, I. Fiete, K. M. Harris, M. Helmstaedter, V. Jain *et al.*, "The mind of a mouse," *Cell*, vol. 182, no. 6, pp. 1372–1376, 2020.
- [15] A. Kirillov, E. Mintun, N. Ravi, H. Mao, C. Rolland, L. Gustafson, T. Xiao, S. Whitehead, A. C. Berg, W.-Y. Lo *et al.*, "Segment anything," *arXiv preprint arXiv:2304.02643*, 2023.
- [16] J. Yang, M. Gao, Z. Li, S. Gao, F. Wang, and F. Zheng, "Track anything: Segment anything meets videos," *arXiv preprint arXiv:2304.11968*, 2023.
- [17] K. Lee, N. Turner, T. Macrina, J. Wu, R. Lu, and H. S. Seung, "Convolutional nets for reconstructing neural circuits from brain images acquired by serial section electron microscopy," *Current opinion in neurobiology*, vol. 55, pp. 188–198, 2019.

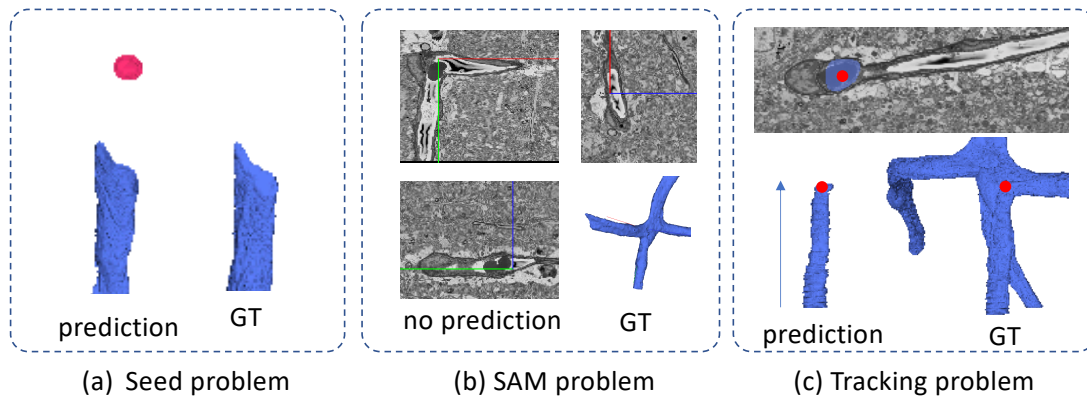


Fig. 12. The failure cases of the proposed method. Three prediction and ground truth pairs are shown.

- [18] J. Wu, Y. Li, N. Gupta, K. Shinomiya, P. Gunn, A. Polilov, H. Pfister, D. Chklovskii, and D. Wei, "An out-of-domain synapse detection challenge for microwasp brain connectomes," *arXiv preprint arXiv:2302.00545*, 2023.
- [19] N. L. Turner, K. Lee, R. Lu, J. Wu, D. Ih, and H. S. Seung, "Synaptic partner assignment using attentional voxel association networks," in *2020 IEEE 17th International Symposium on Biomedical Imaging (ISBI)*. IEEE, 2020, pp. 1–5.
- [20] J. Buhmann, A. Sheridan, C. Malin-Mayor, P. Schlegel, S. Gerhard, T. Kazimiers, R. Krause, T. M. Nguyen, L. Heinrich, W.-C. A. Lee *et al.*, "Automatic detection of synaptic partners in a whole-brain drosophila electron microscopy data set," *Nature methods*, vol. 18, no. 7, pp. 771–774, 2021.
- [21] G. Tetteh, V. Efremov, N. D. Forkert, M. Schneider, J. Kirschke, B. Weber, C. Zimmer, M. Piraud, and B. H. Menze, "Deepvesselnet: Vessel segmentation, centerline prediction, and bifurcation detection in 3-d angiographic volumes," *Frontiers in Neuroscience*, vol. 14, p. 1285, 2020.
- [22] M. Livne, J. Rieger, O. U. Aydin, A. A. Taha, E. M. Akay, T. Kossen, J. Sobesky, J. D. Kelleher, K. Hildebrand, D. Frey *et al.*, "A u-net deep learning framework for high performance vessel segmentation in patients with cerebrovascular disease," *Frontiers in neuroscience*, vol. 13, p. 97, 2019.
- [23] Ö. Çiçek, A. Abdulkadir, S. S. Lienkamp, T. Brox, and O. Ronneberger, "3d u-net: learning dense volumetric segmentation from sparse annotation," in *Medical Image Computing and Computer-Assisted Intervention—MICCAI 2016: 19th International Conference, Athens, Greece, October 17–21, 2016, Proceedings, Part II 19*. Springer, 2016, pp. 424–432.
- [24] V. N. Dang, F. Galati, R. Cortese, G. Di Giacomo, V. Marconetto, P. Mathur, K. Lekadir, M. Lorenzi, F. Prados, and M. A. Zuluaga, "Vessel-captcha: an efficient learning framework for vessel annotation and segmentation," *Medical Image Analysis*, vol. 75, p. 102263, 2022.
- [25] L. R. Dice, "Measures of the amount of ecologic association between species," *Ecology*, vol. 26, no. 3, pp. 297–302, 1945.
- [26] C. Metz, M. Schaap, T. van Walsum, A. van der Giessen, A. Weustink, N. Mollet, G. Krestin, and W. Niessen, "3d segmentation in the clinic: A grand challenge ii-coronary artery tracking," *Insight Journal*, vol. 1, no. 5, p. 6, 2008.
- [27] Y. Cheng, L. Li, Y. Xu, X. Li, Z. Yang, W. Wang, and Y. Yang, "Segment and track anything," *arXiv preprint arXiv:2305.06558*, 2023.
- [28] T. Yu, R. Feng, R. Feng, J. Liu, X. Jin, W. Zeng, and Z. Chen, "Inpaint anything: Segment anything meets image inpainting," *arXiv preprint arXiv:2304.06790*, 2023.
- [29] J. Ma and B. Wang, "Segment anything in medical images," *arXiv preprint arXiv:2304.12306*, 2023.
- [30] R. Deng, C. Cui, Q. Liu, T. Yao, L. W. Remedios, S. Bao, B. A. Landman, L. E. Wheless, L. A. Coburn, K. T. Wilson *et al.*, "Segment anything model (sam) for digital pathology: Assess zero-shot segmentation on whole slide imaging," *arXiv preprint arXiv:2304.04155*, 2023.
- [31] J. Yao, X. Wang, L. Ye, and W. Liu, "Matte anything: Interactive natural image matting with segment anything models," *arXiv preprint arXiv:2306.04121*, 2023.
- [32] Z. Lu, Z. Xiao, J. Bai, Z. Xiong, and X. Wang, "Can sam boost video super-resolution?" *arXiv preprint arXiv:2305.06524*, 2023.
- [33] Y. Liu, L. Kong, J. Cen, R. Chen, W. Zhang, L. Pan, K. Chen, and Z. Liu, "Segment any point cloud sequences by distilling vision foundation models," *arXiv preprint arXiv:2306.09347*, 2023.
- [34] S. Gao, Z. Lin, X. Xie, P. Zhou, M.-M. Cheng, and S. Yan, "Editanything: Empowering unparalleled flexibility in image editing and generation," in *Proceedings of the 31st ACM International Conference on Multimedia, Demo track*, 2023.
- [35] X. Zhao, W. Ding, Y. An, Y. Du, T. Yu, M. Li, M. Tang, and J. Wang, "Fast segment anything," *arXiv preprint arXiv:2306.12156*, 2023.
- [36] C. Zhang, D. Han, Y. Qiao, J. U. Kim, S.-H. Bae, S. Lee, and C. S. Hong, "Faster segment anything: Towards lightweight sam for mobile applications," *arXiv preprint arXiv:2306.14289*, 2023.
- [37] T. Chen, L. Zhu, C. Ding, R. Cao, S. Zhang, Y. Wang, Z. Li, L. Sun, P. Mao, and Y. Zang, "Sam fails to segment anything?—sam-adapter: Adapting sam in underperformed scenes: Camouflage, shadow, and more," *arXiv preprint arXiv:2304.09148*, 2023.
- [38] A. Archit, S. Nair, N. Khalid, P. Hilt, V. Rajashekar, M. Freitag, S. Gupta, A. Dengel, S. Ahmed, and C. Pape, "Segment anything for microscopy," *bioRxiv*, pp. 2023–08, 2023.
- [39] S. Gong, Y. Zhong, W. Ma, J. Li, Z. Wang, J. Zhang, P.-A. Heng, and Q. Dou, "3dsam-adapter: Holistic adaptation of sam from 2d to 3d for promptable medical image segmentation," *arXiv preprint arXiv:2306.13465*, 2023.
- [40] M. A. Mazurowski, H. Dong, H. Gu, J. Yang, N. Konz, and Y. Zhang, "Segment anything model for medical image analysis: an experimental study," *Medical Image Analysis*, vol. 89, p. 102918, 2023.
- [41] J. Cheng, J. Ye, Z. Deng, J. Chen, T. Li, H. Wang, Y. Su, Z. Huang, J. Chen, L. Jiang *et al.*, "Sam-med2d," *arXiv preprint arXiv:2308.16184*, 2023.
- [42] J. Wu, R. Fu, H. Fang, Y. Liu, Z. Wang, Y. Xu, Y. Jin, and T. Arbel, "Medical sam adapter: Adapting segment anything model for medical image segmentation," *arXiv preprint arXiv:2304.12620*, 2023.
- [43] S. Loomba, J. Straehle, V. Gangadharan, N. Heike, A. Khalifa, A. Motta, N. Ju, M. Sievers, J. Gempt, H. S. Meyer *et al.*, "Connectomic comparison of mouse and human cortex," *Science*, vol. 377, no. 6602, p. eabo0924, 2022.
- [44] D. R. Berger, H. S. Seung, and J. W. Lichtman, "Vast (volume annotation and segmentation tool): efficient manual and semi-automatic labeling of large 3d image stacks," *Frontiers in neural circuits*, vol. 12, p. 88, 2018.
- [45] W. Silversmith, J. Bae, P. Li, and A. Wilson, "Kimimaro: Skeletonize densely labeled 3d image segmentations," *Zenodo https://doi.org/10.5281/zenodo*, vol. 5539912, 2021.
- [46] M. Weigert, U. Schmidt, R. Haase, K. Sugawara, and G. Myers, "Star-convex polyhedra for 3d object detection and segmentation in microscopy," in *Proceedings of the IEEE/CVF winter conference on applications of computer vision*, 2020, pp. 3666–3673.
- [47] R. Xie, K. Pang, G. D. Bader, and B. Wang, "Maester: Masked autoencoder guided segmentation at pixel resolution for accurate, self-supervised subcellular structure recognition," in *Proceedings of the IEEE/CVF Conference on Computer Vision and Pattern Recognition*, 2023, pp. 3292–3301.
- [48] F. Isensee, P. F. Jaeger, S. A. Kohl, J. Petersen, and K. H. Maier-Hein, "nnu-net: a self-configuring method for deep learning-based biomedical image segmentation," *Nature methods*, vol. 18, no. 2, pp. 203–211, 2021.

- [49] A. Archit, S. Nair, N. Khalid, P. Hilt, V. Rajashekar, M. Freitag, S. Gupta, A. R. Dengel, S. Ahmed, and C. Pape, "Segment anything for microscopy," *bioRxiv*, 2023. [Online]. Available: <https://api.semanticscholar.org/CorpusID:261125076>
- [50] A. Wolny, L. Cerrone, A. Vijayan, R. Tofanelli, A. V. Barro, M. Louveaux, C. Wenzl, S. Strauss, D. Wilson-Sánchez, R. Lymbouridou, S. S. Steigleder, C. Pape, A. Bailoni, S. Duran-Nebreda, G. W. Bassel, J. U. Lohmann, M. Tsiantis, F. A. Hamprecht, K. Schneitz, A. Maizel, and A. Kreshuk, "Accurate and versatile 3d segmentation of plant tissues at cellular resolution," *eLife*, vol. 9, p. e57613, jul 2020. [Online]. Available: <https://doi.org/10.7554/eLife.57613>